Research Article | Vol. 34, No. 23 / 16 Nov 2026 / Optics Express 45064
Optics EXPRESS

Quantifying light coupling to guided modes in semiconductor slabs with arbitrary scattering patterns

ALEX LAMBERTZ,[1,2,4] ESTHER ALARCON-LLADO,[1,3,5] AND JORIK VAN DE GROEP[2,*]

[1] Center for Nanophotonics, AMOLF, Science Park 104, 1098XG, Amsterdam, The Netherlands
[2] Van der Waals–Zeeman Institute, Institute of Physics, University of Amsterdam, Science Park 904, 1098XH, Amsterdam, The Netherlands
[3] Van 't Hoff Institute for Molecular Sciences, University of Amsterdam, Science Park 904, 1098XH, Amsterdam, The Netherlands
[4] lambertz@amolf.nl
[5] e.alarconllado@amolf.nl
[*] j.vandegroep@uva.nl

Abstract: Optimizing broadband optical absorption in thin semiconductor layers using nanopatterned light-trapping structures remains a major challenge, as the applicability of existing models is restricted. When absorbing layers are thinned to the wavelength scale, guided mode bands discretize and statistical limits are no longer applicable. Coupled-mode theory can make accurate predictions for narrow-band excitation of structures with only a few sufficiently separated modes in order to determine a suitable periodicity, but when localized resonances are introduced in the scattering unit and resonant peaks start overlapping, no further design directives are extractable from it. Here, we present what is believed to be a new post-processing framework applied to standard FDTD simulations to obtain quantitative information from full-field simulations on the energy- and momentum-resolved scattering and absorption distributions for both periodic and arbitrary non-periodic nanopatterns. This enables tailoring of the pattern parameters to steer light into specific guided modes and analyze their absorptive properties and trapping capabilities. We demonstrate the applicability of this toolbox using three case studies in which we assess the impact of localized Mie resonances and (quasi-)random structural correlations on the modal absorption, separate Beer-Lambert and Fabry-Perót contributions to absorption from coupling to guided modes, and quantify coupling — and loss rates of individual modes. These key insights allow significant reduction of the design space and aid in the rational design of many optoelectronic device applications. The framework is broadly applicable across photonics: any structure in which the optical response is to be decomposed into guided-mode contributions — LEDs, thermal emitters, plasmonic sensors, or solar cells — can benefit from this methodology.

© 2026 Optica Publishing Group under the terms of the Optica Open Access Publishing Agreement

1. Introduction

Light absorption in semiconductor substrates poses an important challenge that underlies a wide range of modern optoelectronic technologies. In particular, for applications where the substrate is thinner than the absorption length of light, it becomes critical to modify the light-matter interaction beyond simple refraction by introducing sub-wavelength nanostructures on the surface of the substrate. In fact, such nanopatterned light scattering layers crucially combine their function as anti-reflection coating with their ability to trap light inside the thin absorber substrate to maximally enhance the optical absorption. While optimization routines for their nanoscale geometry have become well established for monochromatic conditions (e.g., light-emitting diodes (LEDs) [1,2], photonic power converters [3,4], or grating couplers [5,6]), optimizing the combined anti-reflection and light trapping properties for broadband illumination conditions

#603898 https://doi.org/10.1364/OE.603898
Journal © 2026 Received 7 May 2026; revised 8 Sep 2026; accepted 30 Oct 2026; published 13 Nov 2026

Optics EXPRESS

remains remarkably challenging. At the same time, it directly impacts the performance of broadband optoelectronic devices, including photo-detectors [7–9], multi-color LEDs [10–12], and photovoltaics [13–15].

Light trapping occurs when incident waves are scattered into the plane of the substrate with in-plane momentum components $k_{\parallel}$ larger than the free-space wave vector $k_0 < k_{\parallel} \leq k_{\mathrm{Mat}}$, i.e., into the guided mode regime, where $k_{\mathrm{Mat}} = 2\pi n_{\mathrm{Mat}} \lambda^{-1}$ denotes the wave vector inside the material with refractive index n_{Mat} at free-space wavelength λ. When the thickness of the material is reduced, the continuum of optical states transitions into a finite number of distinct modes. As a consequence, not all photons that attain a $k_{\parallel}$ within the above interval through diffraction will be effectively trapped and optical absorption is inefficient. As such, light scattering into the plane of the absorber needs to be tailored to the modal structure at each photon energy. Furthermore, since each mode is characterized by a specific dispersive absorption rate, targeting specific modes is key yet often elusive, since the modal dispersion of a full device stack involving multiple layers and nanostructures is not easily obtained.

In literature, the several prototypical geometries have been explored extensively, namely complete order (i.e., periodic gratings) or disorder (fully random). Random roughening techniques such as pyramidal texturing [16] and sandblasting [17] are facile to fabricate but offer little control over the unit cell and size. Instead, to achieve better control, identical unit elements, such as pillars, holes, and non-isotropic shapes, are tailored geometrically to support Mie- [18] or plasmon resonances [19] and placed in optimized (periodic) arrangements [20–23]. There are several models to describe the scattering response of such prototypical geometries, which typically explore an ultimate upper limit for absorption under a restrictive set of assumptions. For thick and weakly-absorbing substrates with random textures, the statistical (Yablonovitch) $4n^2$-limit describes the thermodynamic maximum of optical absorptance. This limit has later been extended to also include the strongly-absorbing parts of the spectrum [24], but crucially assumes a continuum of states as well as uniform population of all optical states and is therefore restricted to thick absorbing layers only.

For thin substrates on the other hand, where modal overlap can be neglected, temporal coupled-mode theory (CMT) can find an upper limit for absorption with periodic patterns [25]. The predicted ultimate absorption enhancement is intrinsically narrow-band, and is greatly reduced when broadband enhancement is considered [26]. Furthermore, absorptance is strongly overestimated when the thickness or periodicity is increased and resonances start to overlap. To address this, a model that accommodates overlapping resonances was developed recently [27]. This presents a major step forward to retrieve accurate predictions for the actual absorption enhancements rather than deriving an upper limit for it. Despite its applicability to absorber thicknesses in-between the restrictive cases mentioned above, the model applies only to periodic structures, ignores the scattering properties of the individual nanostructures within the unit cell, assumes equal coupling rates to all modes and a bulk-like density of optical states that neglects the specific mode structure of the device. These simplifying assumptions often obscure intricate relations between absorption and coupling rates, which give rise to large discrepancies between the model's predictions and experiments.

More recently, structures other than fully random or periodic — such as correlated random or disordered hyper-uniformity — have been proposed [28] and initial experiments demonstrate enhanced optical absorption by matching the pattern's spatial frequencies to the modes supported in the thin substrates [29–32]. In this context, there are no models available that accommodate such tailored patterns and go beyond the assumptions described above. As a consequence, finite-element methods which solve Maxwell's equations in spatially and temporally discretized full-wave simulation volume are commonly employed. Forward-design optimizations therein typically employ a single figure of merit (e.g., total absorptance over a spectral range) while varying a range of free parameters, which makes the process computationally expensive and

Optics EXPRESS

opaque. At the same time, electromagnetic field data obtained from such simulations contain crucial information that can be leveraged to elucidate the role of the scattering unit cell, the arrangement of scatterers, and the geometry of the active layer.

Here, we present a post-processing pipeline that employs energy-momentum resolved absorption data retrieved from full-field simulations to offer quantitative insights into mode-resolved absorption and coupling properties. By "toolbox" we refer to the complete post-processing pipeline applied to standard FDTD simulations (the individual modules are enumerated in the Methods); its novelty lies not in any single step — FDTD, Fourier transforms, and peak finding are all well established — but in how they are combined to simultaneously extract dispersion *and* per-mode coupling rates for arbitrary, including disordered, patterns, without any analytical model of the scatterer geometry. It is compatible with arbitrary (non-periodic) scatterer layouts of considerable size and realistic finite — absorbing — substrate effects, free of restrictive assumptions, and enables physically interpretable optimization beyond brute-force absorptance optimization sweeps. To illustrate its use, we first compare the energy-momentum resolved scattering spectra of a periodic structure on a semi-infinite lossless substrate versus a finite absorptive substrate, and extract mode-resolved absorption efficiencies. Next, we use the toolbox to: (i) investigate the impact of localized resonances within the scattering pattern on the modal absorptance; (ii) study modal coupling in aperiodic (Poisson random and hyperuniform) scattering arrays; and (iii) extract modal properties and coupling rates directly from the absorption heatmaps. Numerical quantification of mode-resolved coupling efficiencies, trapping, and absorptive properties offered by our toolbox provides actionable guidance for the design of device-optimized broadband light-scattering nanopatterns and offers data to refine and validate (semi-)analytical models and their assumptions.

2. Results

To illustrate the problem, we consider the generic case of a plane wave incident on a finite, weakly-absorbing substrate situated on a perfect mirror (Fig. 1). For a flat slab (panel a), light impinges perpendicular to the interface and is partly reflected by the front surface and partially transmitted into the substrate. Since the substrate is weakly absorbing, a considerable fraction reaches the perfect mirror at the bottom, where it is reflected. The reflected wave reaches again the top interface, where it is partially transmitted and reflected again. Interference between the downwards and upwards traveling waves gives rise to Fabry-Pérot oscillations in the absorptance (Fig. 1(c), black) and reflectance spectra, which enhance absorptance at certain wavelengths. All partial waves retain their parallel wave vector (in-plane momentum) in all parts of the system.

A common approach to enhance the optical absorption is to include a periodic corrugation to the top interface (panel b). Indeed, the absorptance (Fig. 1(c), green) and reflectance spectra are greatly modified by diffraction. The interaction of the normally incident light with the patterned layer imparts interface-parallel momentum components to the scattered waves. Due to the periodicity ($p = 350\,\mathrm{nm}$), in-plane momenta changes occur in quanta of $\Delta k_{\parallel} = \sqrt{(2\pi m/p_x)^2 + (2\pi n/p_y)^2}$, where $m, n \in \{0, 1, 2, ...\}$ and $p_x = p_y = p$ in a square lattice with periodicities p_x, p_y along the orthogonal directions x and y, respectively. Comparing the absorptance spectra between these cases (Fig. 1(c)), we observe a substantial broad-band improvement at photon energies E_{ph}>1.5 eV for the patterned slab, while both spectra show similar values at low energies, with the exception of a series of sharp peaks.

To identify the origin of these peaks, one may compare the guided modes supported by the bare substrate in air with the in-plane momentum offered by the periodic structure (Fig. 1(d)). At their intersection, in-plane momentum matching of a diffraction order of the grating a guided mode is fulfilled, and incident light is coupled to the guided mode to form a guided-mode resonance (GMR) [33]. The scattering efficiency and coupling to such GMRs at each photon

Optics EXPRESS

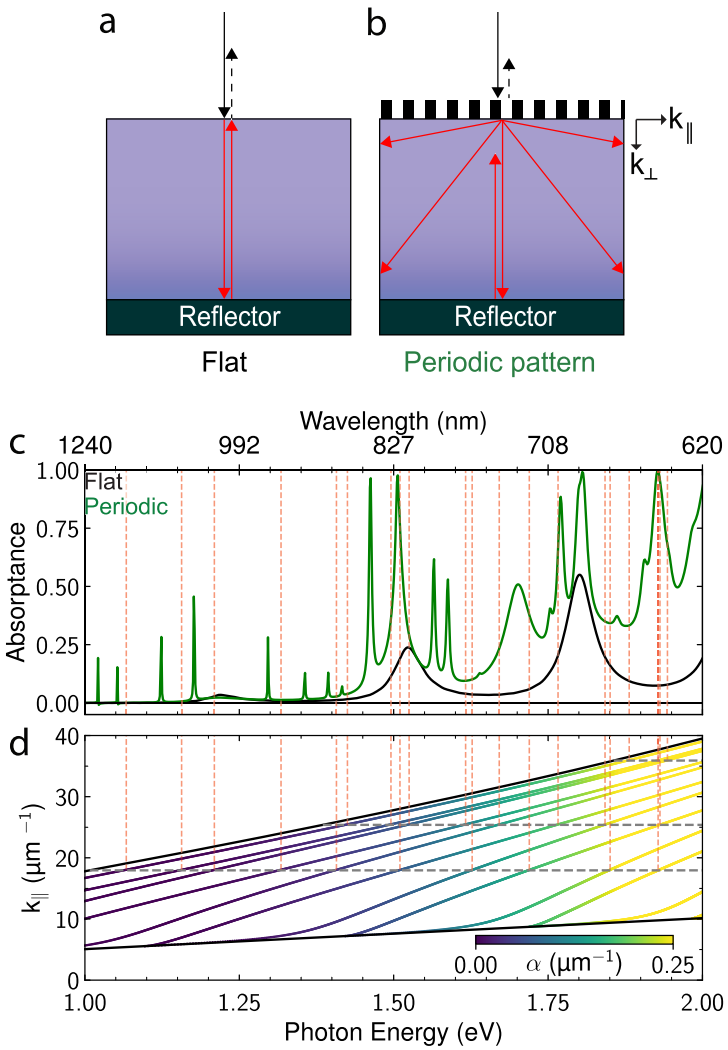

Fig. 1. Illustration of light trapping in ultra-thin weakly absorbing substrates. Illustration of a plane wave incident onto a weakly-absorbing slab on a perfect mirror, where the slab surface is either flat (a) of periodically patterned (b). (c) Full-wave FDTD-calculated absorptance spectra for a 500 nm-thick Si slab on a mirror for a flat (black) and periodically patterned (green) top surface with period $p = 350$ nm. (d) Dispersion diagram of the 500 nm c-Si slab in air. The lower/upper black solid lines represent the light line in air and silicon, respectively. In between these lies the guided-mode regime, where the colored lines correspond to the dispersion curves of the modes, with the color indicating their dispersive absorption coefficient $\alpha(\omega, k_\parallel)$. Horizontal dashed lines correspond to diffraction orders of the square-lattice periodic grating. Vertical dashed lines originate at the intersections of the diffraction orders with guided modes of the unperturbed slab, where guided-mode resonances are expected to occur based on pure momentum matching.

Optics EXPRESS

energy crucially depends on the scattering layer properties, such as unit-cell geometry and area filling fraction, leading to greatly varying coupling rates (γ_e) across the energy spectrum. At the same time, the intrinsic loss rate (γ_i; corresponding to optical absorption) equally depends on photon energy and the momentum of the individual modes through the group velocity (v_g): $\gamma_i = \alpha_m \cdot v_g$ [34]. Here, α_m is the mode's absorption coefficient, which is color coded in Fig. 1(d).

Interestingly, comparing the absorption peaks in Fig. 1(c) with the crossings in Fig. 1(d) shows that the GMR peaks are clearly displaced from the crossing points. The observed spectral shifts result from the modified modal dispersion due to the nanopatterned grating on top of the absorber, which is neglected in simple mode solvers. While the modal dispersion in the presence of such corrugations can in principle be retrieved under specific assumptions, the coupling rate to specific GMRs cannot. These specific assumptions are: (i) a weak corrugation depth relative to the slab thickness; (ii) a known or approximately periodic surface pattern; and (iii) the validity of first-order perturbation theory for the dielectric contrast; under these conditions, standard Bloch-mode or plane-wave expansion methods recover an approximate dispersion relation $\omega(k_\parallel)$. The coupling rates, however, cannot be determined under the same assumptions, because the perturbation theory yields only the shifted eigenfrequencies — it does not provide the overlap integral between the external plane-wave field and each guided mode that is required to determine the coupling rate γ_e. Our method circumvents this limitation by post-processing power-dissipation data from a full-wave FDTD simulation of the actual structure into momentum- and spectrally-resolved heatmaps, from which both dispersion and coupling rates are extracted simultaneously. Indeed, the large variations in peak height clearly highlight that there are strong variations in the relative rates at which light is coupled in/out of the GMRs and absorbed by the GMR throughout the spectral range of interest. Finally, an additional complication in the description of the scattering properties is the presence of the interference fringes (i.e., Fabry-Pérot), which are commonly ignored in conventional CMT models [25].

This simplified example of a periodic structure on a thin slab already highlights the challenge: wavelength and angle-dependent scattering properties of the individual nanoparticles, strongly varying absorption coefficients, and a non-negligible Fabry-Pérot background oscillations complicate the optical absorption far beyond the realms of established models. Additionally, more complex non-periodic and non-random structure factors for broadband scattering layers further challenge the established models [35]. As such, to optimize light scattering and absorption in such advanced devices approaching the theoretical limits, scattered power and momentum distribution for all photon energies need precise quantification, and the ability to track their dependence on the design parameters becomes crucial.

2.1. Toolbox for light trapping analysis

Here, we propose a post-processing pipeline that enables detailed quantification of energy and momentum-resolved light absorption in arbitrarily complex scattering layers and systems. The methodology is outlined as follows: the device layers are set up in a FDTD simulation environment (Fig. 2(a)). The source injects a plane wave towards the stack, which is absorbed either by materials in the stack or the perfectly-matched layer (PML) boundary located above the source plane. Electromagnetic fields are calculated in discrete time intervals until the residual energy residing in the system falls below a predetermined auto-shutoff threshold (see Methods). Two monitors are used to record the local electromagnetic fields and energy flux in reflectance (between the PML and source) and inside the flat absorbing layer close to the scattering interface where light is transmitted into the substrate. Since only the net transmitted power is stored in the monitors (the difference between the transmitted power in both directions normal to the monitor plane), the transmittance monitor contains only the power fraction absorbed in the device. Due to its close vicinity to the scattering layer, the recorded power contains both contributions from the evanescent near-fields of the scattering units as well as propagating modes in the uniform

Optics EXPRESS

absorber layer. Next, we perform a near-to-far-field transformation of the transmitted near fields (Fig. 2(b)). In essence, this transformation decomposes the local near-field data into a set of plane waves of different wavevectors. In this step, evanescent portions are omitted and only propagating waves are retained (see Methods). From the coefficients of the basis set of plane waves, we obtain the angular distribution (in-plane momenta $k_{\|}$) of the absorbed power fractions within the absorbing layer (Fig. 2(c)), which resemble a diffraction pattern or back-focal plane image in Fourier space. From this, we calculate the radially-averaged absorptance versus $k_{\|}$-magnitude at each photon energy and display the result in an energy-momentum resolved heatmap (Fig. 2(d)). Crucially, this three-dimensional momentum- and energy-resolved data enables the isolation of individual resonant features that would otherwise be indistinguishable in a regular frequency spectrum, and thereby allows one to compute relevant physical quantities of isolated GMRs, such as propagation constant, absorption coefficient, group velocity, and coupling rates to free space channels.

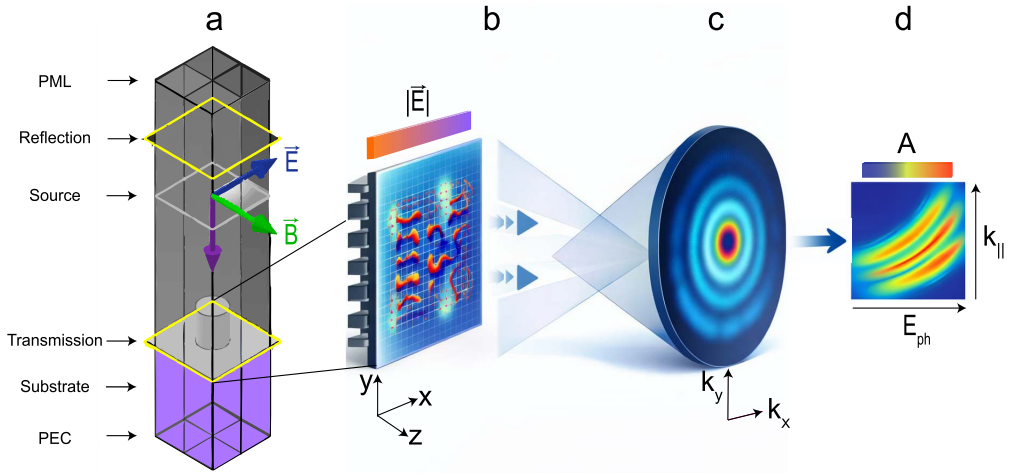

Fig. 2. Methodology to obtain energy and momentum-resolved absorption. (a) Employ finite-difference time-domain simulations to obtain near-field profiles inside the (finite) substrate close to the scattering layer. (b) Perform near- to far-field transform to retrieve propagation properties. (c) Radial averaging of in-plane momentum distribution $|k_{\|}|$ at each photon energy. (d) Integrate scattered power into specific momentum channels to display absorptance and coupling efficiencies for specific guided modes.

We note that established electromagnetic toolkits such as RETICOLO [36] and RETOP [37] provide powerful and widely used capabilities for the analysis of structured media. RETOP is a dedicated near-to-far-field transformation tool that can operate on near-field data obtained with rigorous coupled-wave analysis (RCWA), finite-difference and finite-element methods. It enables near-to-far-field transformations in stratified media and allows retrieval of coupling into radiative and guided modes. RETICOLO, based on rigorous coupled-wave analysis, is particularly well suited to periodic or pseudo-periodic structures and offers detailed layer-resolved absorption. MANlite [38] is a solver for quasi-normal modes including absorptive materials. It operates on near-field data sets obtained by the finite-element method and handles finite systems and disorder. In comparison, the present toolkit is designed to address a complementary set of functionalities, namely the resolution of individual modal absorption contributions and explicit coupling rates between free-space and guided-mode channels in arbitrary three-dimensional, dispersive, and non-periodic structures.

Optics EXPRESS

2.2. Principle demonstration

To illustrate the merits of the toolbox, we first study a model system comprised of a square-lattice periodic grating on a non-dispersive and lossless semi-infinite substrate with $n = 3.55$ (Fig. 3(a)). The most fundamental insight is provided by a heatmap that illustrates the light distribution as a function of the in-plane momentum and photon energy in the substrate as a fraction of the incident power upon a single scattering event (b). The white curve denotes the light line in air, which marks the onset of the guided mode regime, and the color represents the fraction of power per unit wavevector normalized to the incoming power at that photon energy. The heatmap shows bright horizontal lines at $k_{\|} = 0$ as well as specific non-zero momentum values.

A periodic grating scatters light exclusively into its corresponding diffraction orders, which, for a square lattice, occur at in-plane momenta given by:

$$k_{\|}^2 = (2\pi i/p)^2 + (2\pi j/p)^2 \,, \tag{1}$$

with $i, j \in [0, \pm 1, \pm 2, ...]$ indicating the diffractive order in the x and y direction, respectively, labeled as (i, j). The power fraction in each diffraction channel reduces with both decreasing photon energy and increasing diffraction order. Comparing Fig. 3(b) with the normalized power spectral density (PSD) of the periodic pattern (Fig. 3(c)) highlights the power diffracted into each order, showing dominant scattering into the $(i, j) = (\pm 1, 0)$ channel. The decrease in power in this channel for lower photon energies results from the wavelength-dependent scattering efficiency of the grating's unit cell.

For light trapping, the total power fraction scattered beyond the light line in air ($\equiv k_c$) is of particular interest. As such, in Fig. 3(d), we integrate and classify power fractions at each photon energy as back-scattered (i.e. reflected, red), scattered into the substrate with $k_{\|} < k_c$ (gray), and scattered beyond the light line with $k_{\|} \geq k_c$ (blue). The shaded regions confirm the observation that at low photon energies, nearly all forward scattered power falls within the escape cone (primarily at $k_{\|} = 0$), while for larger energies, increasingly more power is diffracted into the guided-mode regime. This analysis provides insights into the grating's scattering efficiency and enables a quantitative study of the coupling strength to specific diffraction orders. As such, it enables the de-convolution of the respective impact of the lattice pitch and unit-cell geometry on the angular scattering profile at each photon energy. For a semi-infinite and lossless substrate, this analysis is limited to a single-pass scattering event, and predictions of the exact absorption spectra of a finite absorbing slabs with such periodic patterns remain elusive.

Next, we aim to obtain accurate absorption characteristics for a real thin-film device in which discrete waveguide modes play a central role. As such, we consider a thin (finite) substrate to include the effects of back reflections and interference inside the slab, and also take into account optical absorption in the material. We use the same 500 nm-thick slab of c-Si as an example, and place a non-absorbing and non-dispersive periodic grating on its top surface, as well as a perfect reflector underneath (Fig. 4(a)). In contrast to Fig. 3(b), the color scale in Fig. 4(b) now represents the absolute absorptance that includes multiple scattering events inside of the absorber. To do this, we leverage the fact that the near-field monitor data collection only records net transmitted powers. While the methodology remains unchanged, in the previous example, all power transmitted through the grating was eventually absorbed by the perfect-matched layer (PML) boundary inside of the substrate, thus suppressing any reflection. For a finite absorber, the perfect reflector at the bottom of the layer enables multiple interactions with the scattering layer which enables out-coupling from the substrate. Out-coupled power fractions are subtracted from the monitor data and the remainder solely quantifies power absorbed in the substrate. Our method also handles imperfect back reflectors and absorbing layers besides the active material of interest. The power normalization in this case requires an additional transmission monitor into these layers and is further described in the Method section.

Optics EXPRESS

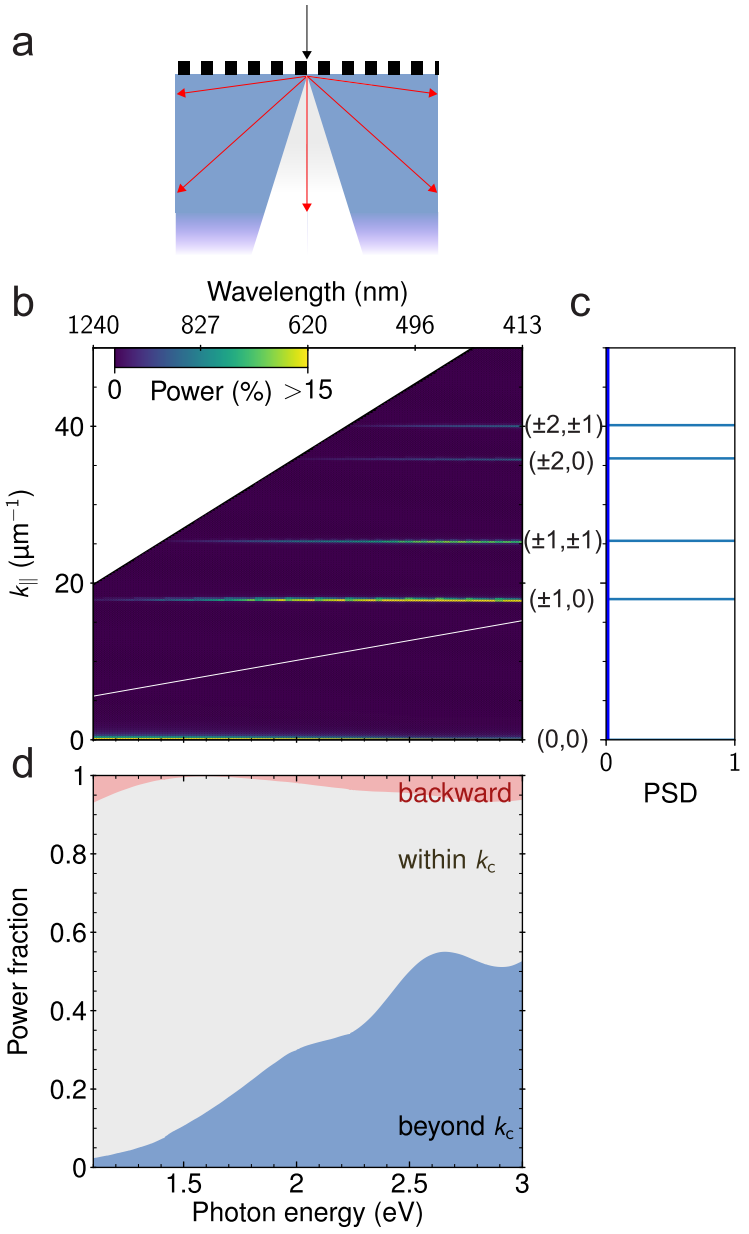

Fig. 3. Momentum-energy resolved scattering efficiency of a periodic grating on a semi-infinite, lossless, and non-dispersive substrate. (a) Schematic of light scattering into a semi-infinite substrate by a periodic grating. The gray cone represents the light cone and blue regions the guided mode regime. (b) Power distribution (color-coded) as a function of in-plane momentum and photon energy of incident light scattered into a semi-infinite, non-absorbing substrate (n = 3.55) by a periodic grating comprised of pillars with radius r_{pillar} = 75 nm, height h_{pillar} = 75 nm, and n_{pillar} = 3.55. At each photon energy, the sum over all momenta equals the transmittance into the substrate and, in the absence of absorption, is equal to (1-R). (c) Normalized power spectral density (PSD) of the periodic grating. The diffraction channels are labeled by their order in the square lattice. (d) Reflectance (red, top) and integrated transmittance within (gray, middle), and beyond the light line (blue, bottom).

Optics EXPRESS

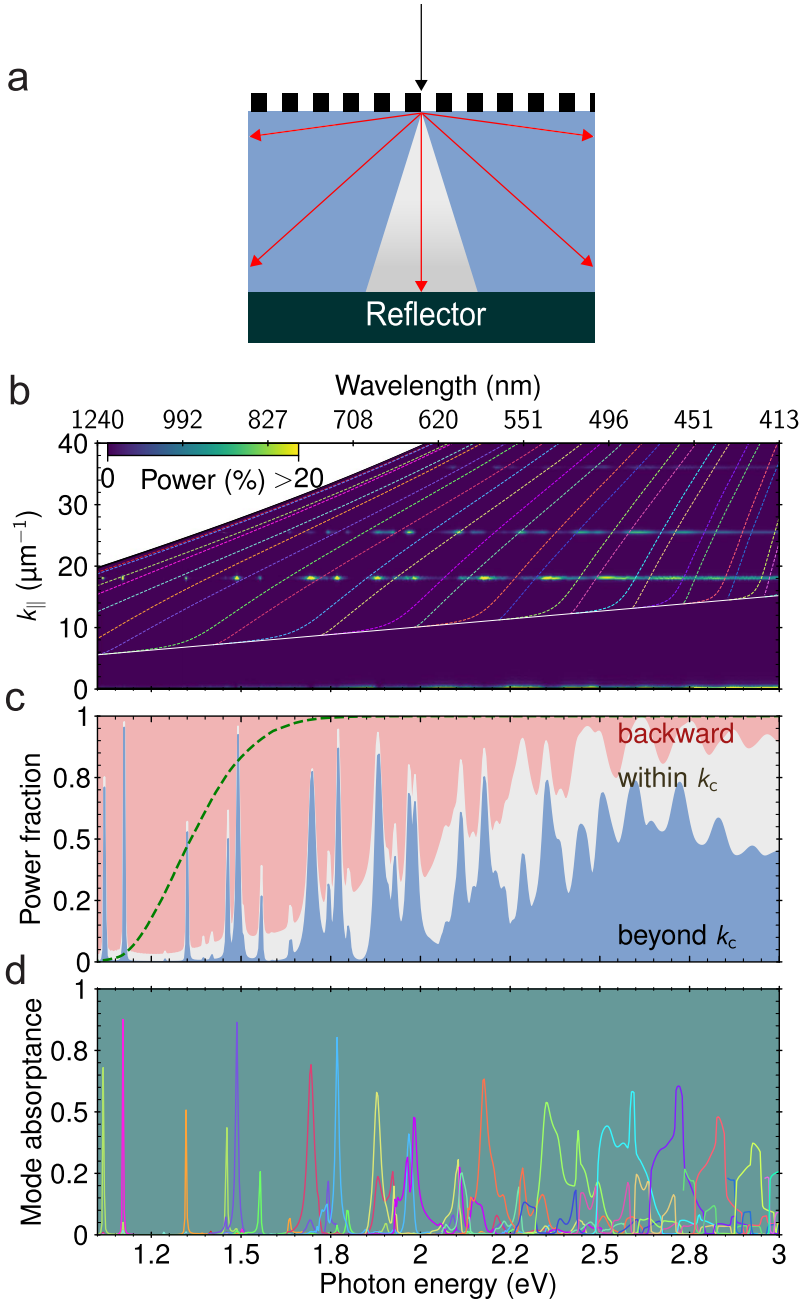

Fig. 4. Absorptance in a 500 nm Si substrate on a PEC with a periodic grating. (a) Schematic of light scattering into the Si substrate on a perfect mirror by a periodic grating. The gray cone represents the light cone and blue regions the guided mode regime. (b) Absorbed power distribution (color-coded) as a function of in-plane momentum and photon energy for a 500 nm silicon slab with periodic grating comprised of pillars with radius r_{pillar} = 75 nm, height h_{pillar} = 75 nm and n_{pillar} = 3.55. (c) Integrated power fractions for reflectance (red), and absorptance for momentum within (gray) and beyond the escape cone (blue). The green dashed line denotes the Lambertian $4n^2$-limit absorption limit in the slab [24]. (d) Extracted modal absorptance highlighting how each individual GMR contributes to the total absorptance in (c). Colors match those in (b).

Optics EXPRESS

The heatmap (Fig. 4(b)) shows similar bright horizontal lines as in Fig. 3(b), yet here they become strongly modulated across the spectrum, and for 1 eV < E_{ph} < 2 eV, they appear as distinct spots only at specific photon energies where momentum matching with the grating reciprocal lattice vector is fulfilled (i.e. crossings of solid and dashed lines in Fig. 1(d)). At these specific locations in the momentum-energy (k-E) plane, light trapping occurs through the resonant excitation of GMRs. The extreme absorptance enhancements beyond 90 %, e.g. at ~ 1.13 eV (Fig. 4(c)), are almost entirely due to scattering beyond the light line, which provides direct further evidence of coupling to these guided modes. Crucially, our numerical analysis enables the integration of the absorptance around distinct spots in the k-E plane to yield the fraction of light absorbed by coupling to the corresponding GMR. This presents the compelling opportunity to identify the (combination of) corresponding guided-mode resonance(s) for each spectral peak and infer their properties using a simple mode solver [39].

To do this, we start with the guided modes of 500 nm c-Si slab in air, which are displayed as dashed lines and overlaid with the heatmap in Fig. 4(b). At each photon energy, we can assign the GMRs to the nearest mode and extract its contribution to total absorption (Fig. 4(d)). Similar to Fig. 1, the presence of the nanopatterned grating modifies the modal properties of the slab, and as such the peaks in absorption due to a GMR are slightly displaced from the mode branches that are calculated without taking the grating into account. The scattering layer with sub-wavelength periodicity gives rise to an effective-medium refractive index [40,41], which red-shifts the guided modes with respect to the assumed air-cladding (i.e., n>1). To take into account this modified modal structure in the analysis, we employ a rationally motivated asymmetric integration environment around each mode in the process of allocating absorbed power to specific modes (see Methods).

We note that the modal decomposition of the absorptance (Fig. 4(d)) aligns well with the peaks observed in Fig. 4(c), where for most GMRs the majority of absorption is attributed to a single mode and supported by higher-order modes only in small amounts. Especially when GMRs occur at different $k_{\|}$ at a similar photon energy (e.g. around 1.9 eV), the decomposition by modal contribution lends valuable insights into the scattering efficiency and provides the means to de-convolute the effect of light trapping from Fabry-Pérot resonances.

These results so far highlight how our numerical toolkit enables momentum-resolved insights in the absorptance for finite and absorptive semiconductor layers, including the contribution of individual GMRs for fully periodic systems that are already well-studied in literature. In the following, we will capitalize on the generic applicability of our post-processing pipeline and turn our attention to scenarios which are non-trivial or otherwise intractable with other approaches. We first study the influence of localized resonances before turning our attention to non-periodic systems with varying degrees of spatial correlations.

2.3. *Case study 1: impact of localized resonances in scattering patterns*

One of the important assumptions in both the statistical analysis of light absorption in randomly textured thick slabs as well as CMT for thin slabs is that the coupling efficiency to all available modes is identical. This assumption is imperative to simplify the theoretical analysis, yet does not take into account the complex frequency- and angular dependent scattering response of the individual nanostructures that comprise most scattering patterns. In this first case study, we investigate the influence of localized resonances on the coupling efficiency to waveguided modes. To this end, we analyze and compare the optical absorption for two different pillar heights in an otherwise unchanged scattering layer (Fig. 5). The pillar dimensions are r = 75 nm, h = 75 nm (left column) and r = 75 nm, h = 175 nm (right column). By increasing the height above ~ 100 nm, vertical electric and magnetic current loops characteristic of localized (Mie) resonances are supported at lower photon energies, which about triples the scattering efficiency and promotes scattering into larger in-plane momentum values [43] (panels a,d). Analogous to

Optics EXPRESS

Fig. 4(c), the area under the curves in Figs. 5(b,e) is subdivided into different shades to denote the fraction of power that is reflected (red), scattered within the escape cone (gray) and beyond (blue). Relative to the total scattering efficiency, the larger pillar scatters more light beyond and less into the escape cone than the smaller pillar, yet at the same time, it shows increased reflectance.

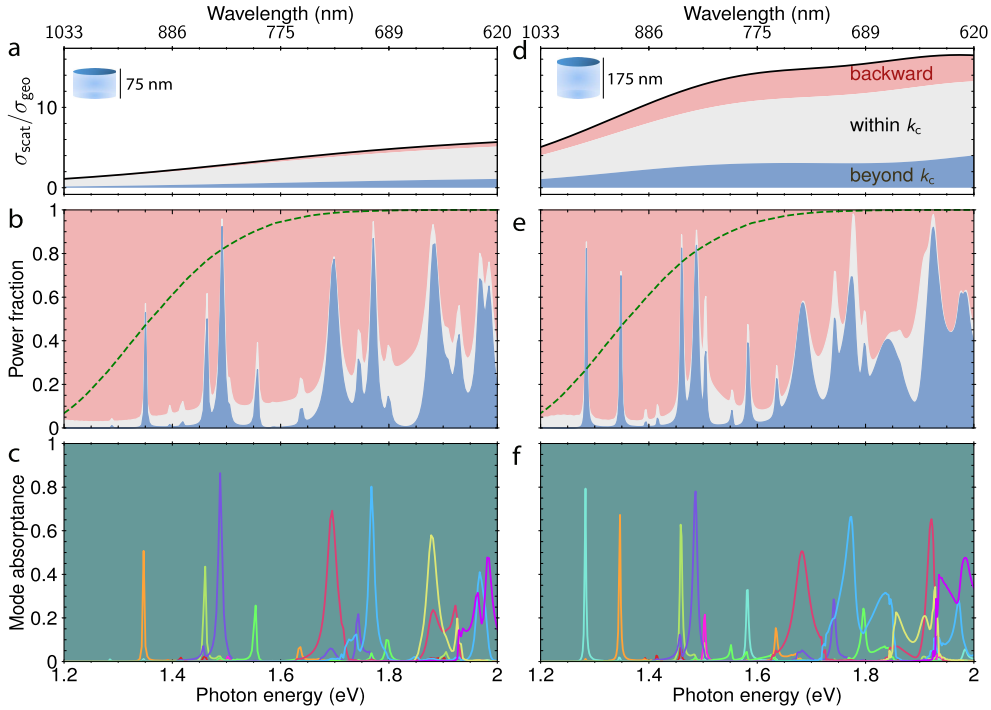

Fig. 5. Effect of localized resonances on periodic scattering patterns. Top row: Direction-resolved scattering cross-sections for a pillar (r = 75 nm, n = 3.55) with heights h = 75 nm (a) and h = 175 nm (d) on a semi-infinite, dispersion-less substrate (n = 3.55). Middle row: Integrated power fractions by momentum and photon energy for back-reflected (red), transmitted into (gray) and beyond (blue) the escape cone for the shorter (b) and taller (e) pillar in a square lattice (p = 350 nm). Green dashed curve denotes the Lambertian $4n^2$-limit [42]. Bottom row: Modal decomposition versus photon energy for short (c) and tall (f) pillar.

In the integrated power fractions (Figs. 5(b),(e)) and as a consequence of the increased pillar height, the peak absorption for most GMR changes and additional peaks appear. As a result, the GMR peak occurring at ~ 1.28 eV, which is hardly noticeable for h = 75 nm (Fig. 5(b)), becomes strongly pronounced in Fig. 5(e) with a single mode contributing ~ 80 $\%_{abs}$ to the total absorptance. In contrast to that, the absorption peak at ~ 1.48 eV (purple) decreases in height as the pillar height increases.

Despite being limited in applicability in its conventional form, CMT does offer a very valuable framework to assess the coupling conditions for a single isolated GMR, yet does not apply to strongly overlapping resonance peaks in the absorption spectra. Here, we capitalize on the energy- and momentum-resolved information from the toolbox, which allows one to isolate single resonances by their $k_{||}$ dependence and in turn, apply the coupled-mode formalism. The amplitude of a GMR in the frequency domain is typically described by a form of the temporal coupled-mode theory equation [25,44]:

$$A(\omega) = \frac{\gamma_i \gamma_e}{(\omega - \omega_0)^2 + (\gamma_i + N\gamma_e)^2 / 4}, \tag{2}$$

Optics EXPRESS

with loss-rates γ_i due to internal absorption, and γ_e due to coupling to N free-space channels, at driving frequency ω and with resonance frequency ω_0.

According to Eq. (2), the GMR amplitude is governed by the ratio of flux rates γ_e of the N input/output ports and the intrinsic loss γ_i of the mode. At critical coupling, i.e., $\gamma_i = N\gamma_e$, unity absorptance can be achieved. In broadband optoelectronic devices, one typically achieves the highest averaged absorptance across the spectrum when the system is operated in the over-coupling regime [27]. However, to achieve (near-)unity absorption at resonant frequencies, one would target critical coupling instead. The external coupling rate γ_e increases with the pillar height while the intrinsic loss remains unchanged. The diminution of the absorption peak at ~ 1.48 eV as a result of increased pillar height is thus indicative of a transition from close to critical coupling to the over-coupling regime $N\gamma_e > \gamma_i$, leading to reduced absorptance of the GMR. Overall, the momentum-resolved analysis of our toolbox thus offers the ability to analyze the impact of geometrical changes (e.g., particle height) on the coupling and absorption properties of individual GMRs.

The light trapping observed in both examples can yield absorptance beyond the Lambertian $4n^2$-limit [42] (green dashed curves in Figs. 5(b),(e) as predicted by coupled-mode theory [25,26], yet the effect is of narrow-band character and the averaged absorptance stays far below this limit. As evidenced by Figs. 4 and 5, such a periodic grating, despite being sub-wavelength in its lattice parameter, does not afford a broad-band light trapping effect that is desirable in many optoelectronic applications including thin-film solar cells. In fact, significant absorption enhancement by light trapping is limited to the number of momentum matching conditions between guided-mode branches and diffraction orders.

2.4. Case study 2: modal coupling in aperiodic scattering arrays

In order to obtain absorption enhancements that are truly broad-band in nature, it is necessary to avoid patterns with extreme degrees of order and instead regard nanostructures with continuous PSD features, such as random or correlated-disordered systems. As such, we will now apply our toolbox to two distinct cases of aperiodic systems that exhibit continuous features in their PSD (see middle column in Fig. 6), and thereby can couple incident light to intervals of in-plane momenta rather than single discrete values. Retrieving the modal absorption for such non-periodic structures on thin absorbing slabs lies well beyond what statistical and CMT models can offer, and as such poses a unique model system to assess the capabilities of the post-processing pipeline.

The left column in Fig. 6 considers a Poisson-random distribution of pillars with $r = 75$ nm and $h = 175$ nm. The random real-space locations of pillars (a) translates to a continuous PSD profile, which decays slowly towards large in-plane momentum vectors $k_\parallel$. The continuous PSD features, in principle, scatter light into all available $k_\parallel$-channels, thus covering the escape cone and guided-mode regime. In the momentum-resolved absorptance heatmap versus photon energy (Fig. 6(b)), absorptance profiles in the guided mode regime appear markedly different from the periodic case (Fig. 4). Here, the absorptance profile shows distinct bright lines, revealing enhanced absorption profiles that follow the dispersion of the guided modes (Fig. 1(d)). In contrast to the discrete GMR spots for the periodic example, GMRs produced by a random pattern appear as sub-branches to all available guided modes. In fact, momentum matching conditions occur at any in-plane momentum where the PSD of the pattern and guided modes overlap. At photon energies below ~ 1.8 eV, in-plane momentum values suitable for light trapping fall within an interval of $k_\parallel \in [5, 30]\ \mu\text{m}^{-1}$. However, the PSD of the random pattern also features significant intensity for wavevectors outside of this range. Larger in-plane momentum values present in the scattering pattern, on the one hand, contribute to haze [45], and thereby reduce the scattering efficiency into the $k_\parallel$-range of guided modes. Any PSD intensity at $k_\parallel < 5\ \mu\text{m}^{-1}$, on the other hand, leads to scattering within the escape cone and similarly reduces the overall absorptance. As a

Optics EXPRESS

consequence, the integrated power fractions (Fig. 6(c)) show between 30 % and 60 % absorptance and as well as significant fractions within k_c at photon energies 1.4 eV$<E_{ph}<$2 eV.

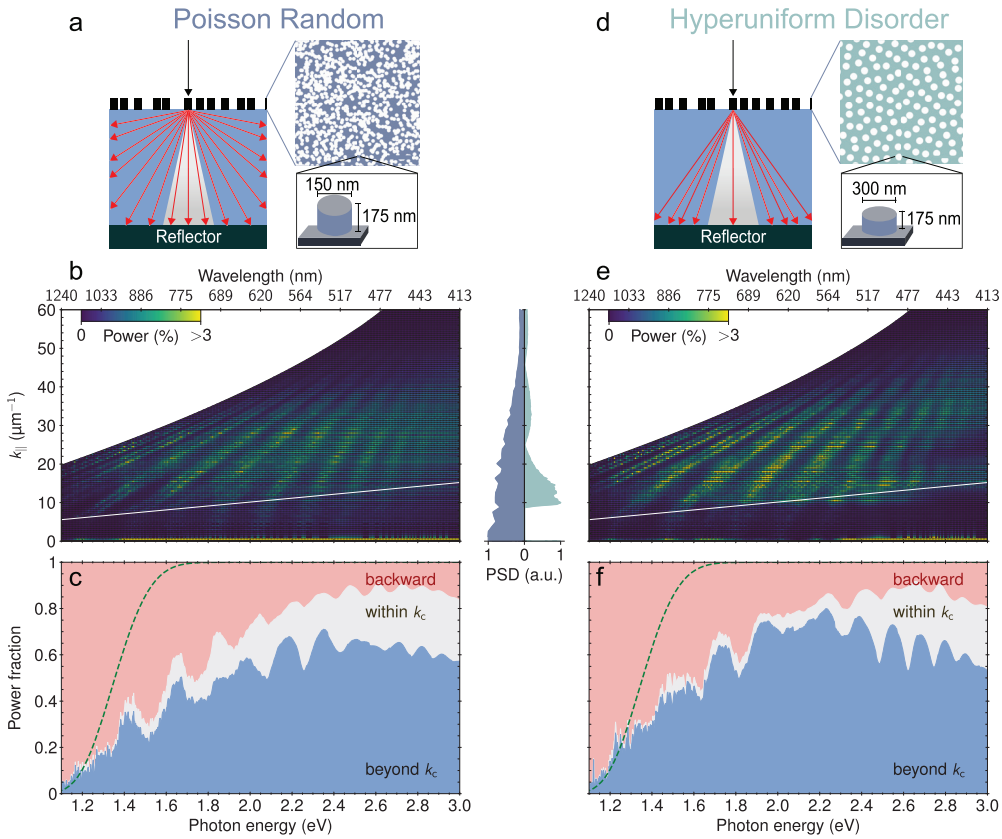

Fig. 6. Energy and momentum resolved absorptance for aperiodic scattering layers. Schematic of light scattering into a finite substrate on a mirror, real-space arrangements of scatterers and the scattering unit cells are shown for a random (a) and a hyperuniform-disordered (d) pattern. Heatmaps (b,e) and integrated power fractions (c,f) for a 500 nm slab of c-Si on a perfect mirror, where the top surface of the silicon is patterned with Poisson-random (a,c) or hyperuniform-disordered (e,f) arrangement of nanopillars with height h = 175 nm, n = 3.55, and conformally coated with a 72 nm anti-reflective layer (n=1.81). PSD of the Poisson-random (blue) and hyperuniform-disordered (green) patterns are shown in the middle column. Green dashed curves in (c,f) represent the Lambertian $4n^2$-limit.

By including some degree of spatial correlations to a random pattern, the PSD can be tailored without compromising its continuous features for large wavevector intervals. A special class of such arrangements exhibits disordered hyper-uniformity, or hyperuniform disorder (HUD), which describes a system featuring randomness at small length scale but suppressed density fluctuations at larger scales, thus producing long-range homogeneity in the absence of Bragg peaks. HUD configurations are classified by a vanishing structure factor $S(k)$ at small momenta, i.e., $S(k) = 0$ for $k \to 0$ [46]. In previous works, HUD patterns have led to record-breaking absorption enhancements in ultra-thin Si layers [29]. They are of particular interest in broad band optical devices due to their inherent ability to tailor occurrences of specific in-plane momentum values and thereby leverage a non-uniform spectral response with varying degrees of spatial correlations.

Optics EXPRESS

In the right column of Fig. 6, we study the absorptance featuring so-called stealthy hyperuniform disorder [28,47]. The term "stealthy" pertains to the property that $S(k) = 0$ for $k_{\parallel} \in [0, k_l]$, meaning that the structure factor is suppressed for all wavevectors up to k_l. The structure factor relates to the PSD via a normalization function and we describe the structural correlations by their PSD, due to its simple calculation via fast-Fourier transform of the real-space images and the inclusion of nanoscale properties of the scattering objects [48]. The real-space pattern and PSD of a particular stealthy HUD configuration are shown in panel d and the middle column (turquoise) of Fig. 6, respectively. Despite the limited number of points in our finite lateral simulation window of 5×5 μm^2, the PSD is strongly suppressed for all $k_{\parallel}$<8 μm^{-1} and most of the intensity is concentrated within the interval $k_{\parallel} \in [9, 18]\,\mu m^{-1}$ (see also Fig. S1 for a comparison of the structure factor and the PSD), which covers the majority of the guided-mode regime down to photon energies of 1 eV. The heatmap (e) reveals that the continuous PSD again results in continuous guided mode resonances that enhance the absorption, similar to the random pattern (Fig. 6(b)). Since the PSD is tailored towards k-values near the Si bandgap, scattering into the GMRs is more efficient than for the random pattern for photon energies up to about 2.2 eV, resulting in strongly enhanced integrated absorption in this spectral range (Fig. 6(f)). In addition, the suppression of small wavevectors results in reduced scattering within the escape cone, which is again corroborated by the small gray-shaded region in the integrated power fractions. Overall, absorptance in the 1.4 eV<E_{ph}<2 eV energy range is increased to (30 − 80) % due to tailored scattering into the guided-mode regime.

A minimum of about 25 particles is needed for spatial correlations to have a noticeable impact on the coupling rates in a simulation environment. As such, optimizing these arrangements for specific applications or devices demands significant computational resources and time, yet provides minimal insight into why certain parameter sets yield better performance than others [49,50]. With our toolkit, the precise contribution to absorption in terms of momentum and energy domains can readily be retrieved and impacts of parameter variations traced to the coupling conditions of individual modes. In the following, we take advantage of the momentum-resolved absorptance maps to extract the propagation-, absorption- and coupling characteristics of individual GMRs directly.

2.5. Case study 3: extracting coupling rates and modal properties

As observed in Fig. 4(b), the modal structure of a device obtained through mode solving of a simplified device layer structure typically provides incorrect dispersion curves. Here, we instead retrieve the modal properties directly from the absorption heatmaps as function of momentum and energy, and analyze the properties of guided-mode resonances in both domains simultaneously. In literature, absorption peaks are generally analyzed in the frequency domain only, and contain information from all accessible in-plane momentum contributions, i.e., from all modes with resonances in the frequency interval $\Delta\omega$ [51–53]. In recent work [29,49,54,55], disordered patterns have been shown to produce strongly overlapping GMR peaks that cannot be de-convoluted by frequency-domain analysis alone. With our approach, we can select small $\Delta k_{\parallel}$-intervals and examine the resonance peak versus photon energy of guided-mode resonances in isolation and extract their specific properties. Hence, the additional dimension of momentum provides a manual circumvention of the common obstacle of overlapping resonance peaks in the absorption spectrum. By combining the information from both domains, we retrieve the mode propagation and absorption parameters directly from the simulation data. Extracted real mode data of this kind allow to gauge (semi-)analytic models, validate their assumptions, analyze the impact of changes that yield identical results (e.g., pillar height), and extend models to previously elusive cases such as non-periodic, correlated-random or other designs featuring more exotic PSDs and (multiple) scatterer geometries.

Optics EXPRESS

As an example, we examine an excerpt (Fig. 7(a)) of the heatmap in Fig. 6(e) and extract slices at 1.247 eV (Fig. 7(b)) and at $k_{\|} = 20.5\,\mu\text{m}^{-1}$ (Fig. 7(c)) and observe GMRs in both energy- and momentum domain separately. The GMR occurring at the crossing of the slices differs significantly in shape and full width at half maximum (FWHM) when viewed in either domain. We fit a series of Lorentzians to the peaks in both domains in order to quantify their properties (dashed lines). The peak position of the lorentzian fits corresponds to the propagation constant β of the mode associated with the GMR, while the FWHM in the energy domain FWHM_e relates to the modal loss rate $\text{FWHM}_\text{e} = 2\gamma_i$. From the quotient of the $\text{FHWM}_{\text{e/m}}$ in the energy-/momentum domain, respectively, we can extract the group velocity $v_\text{G} = \text{d}\omega/\text{d}k \equiv \text{FWHM}_\text{e}/\text{FWHM}_\text{m}$.

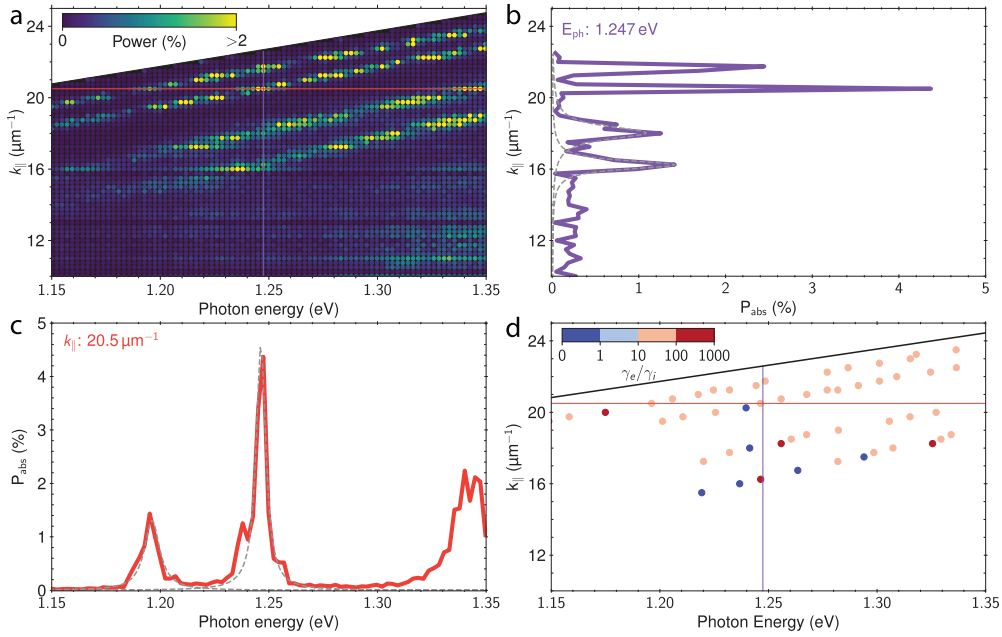

Fig. 7. Retrieving modal dispersion from energy-momentum heatmaps. (a) Excerpt of the heatmap Fig. 6(b) with colored lines indicating slices in momentum- (vertical) and energy space (horizontal) used for (b,c). (b) Slice of $k_{\|}$ versus absorbed power fraction at 1.247 eV with Lorentzians fitted to the GMR peaks (dashed gray curves). (c) Slice of absorbed power fraction versus photon energy at $k_{\|} = 20.5\,\mu\text{m}^{-1}$ and Eq. 2 fitted to the central GMR peak (dashed gray curve). (d) Detected GMR peaks are plotted with color denoting the quotient of the rates γ_e/γ_i (coupling condition), which are extracted from fits such as in (c).

Next, we leverage the fact that a single peak can be isolated and fit Eq. (2) to the GMR peak in the energy domain to extract γ_e, γ_i directly from the simulation. The number of free-space channels N can be included as a fit parameter or set manually. From this, we calculate the coupling condition γ_e/γ_i and use this to color-code the identified GMRs in Fig. 7(d). The PSD of the hyperuniform pattern (Fig. 6) lies exclusively outside of the escape cone in the examined energy range, therefore $N = 1$ is a valid choice for this pattern. We observe that most GMR are moderately over-coupled with $30<\gamma_e/\gamma_i<130$, and only a few detected peaks are under-coupled. None of the peaks are close to critical coupling $\gamma_e/\gamma_i = 1$. As opposed to investigating a single GMR's response to a change in the scattering layer design parameters, Fig. 7(d) reveals the impact for a large collection of GMRs in momentum and energy domains simultaneously. With this method, changes to pattern parameters can be traced to the coupling condition of individual GMR across the entire energy and momentum range, thus providing insightful figures of merit for optimization routines targeting specific applications.

Optics EXPRESS

Altogether, these three examples demonstrate the ability to, on the one hand, analyze the impact of local scatterer geometry on the coupling rates to individual GMRs, and, on the other hand, trace the momentum space distribution of light when scattered by arrangements of scatterers that exhibit complex disordered PSD signatures. Furthermore, we show that by application of the CMT formalism, guided-mode parameters are extractable directly from energy- and momentum-resolved absorptance heatmaps, which allow gauging the predictions of dispersion analysis from analytical models. In the future, we plan to utilize the insights provided by the toolbox to combine individual particle scattering responses with the momentum distribution of their structural arrangement to advance existing models of absorptance and dispersion in complex device architectures.

This mode-resolved picture also clarifies how the approach helps optimization, which is otherwise dominated by black-box figures of merit extracted directly from full-wave simulations. First, it provides physical interpretability: instead of treating absorption as an opaque objective function, the toolbox identifies which modes are responsible for peaks in the absorption spectrum and how strongly each couples (γ_e) versus dissipates internally (γ_i), so an optimizer can target specific modes — e.g., maximize γ_e/γ_i at a given wavelength — rather than blindly maximizing total absorption. Second, it reduces the design space: if, for example, the first two guided modes dominate coupling in the spectral band of interest, only the structural parameters that affect those modes need to be optimized, dramatically reducing the number of degrees of freedom compared to pixel-wise or topology-optimization approaches. For instance, Fig. 5 demonstrates how increasing the pillar height leads to a drastic change in the coupling condition of GMR contribution to absorption at $E_{ph} \sim 1.28\,\mathrm{eV}$ and $E_{ph} \sim 1.35\,\mathrm{eV}$.

3. Conclusions

In summary, we provide a new post-processing approach applied to standard FDTD simulations to study light absorption and coupling to waveguide modes in arbitrary scattering structures on thin semiconductor slabs, enabling quantification of coupling efficiencies well beyond the established frameworks for fully random or periodic structures. Since the numerical method relies solely on a far-field projection of the local electromagnetic fields, this analysis is also applicable to engineered random designs that exhibit correlations over large length scales (up to $5 \times 5\,\mu\mathrm{m}^2$ in this study). Using a periodic geometry as a model system, we reveal the complex momentum- and energy-dependent scattering efficiencies into distinct diffraction channels for semi-infinite and lossless substrate. Next, we highlight how the model offers a quantitative assessment of the absorptance of individual and discrete optical modes in thin semiconductor slabs. We apply the toolkit to three case studies that are incompatible with the assumptions and abilities of existing models. First, we investigate the effect of localized resonances in the periodic unit cell and qualitatively assess their impact on the coupling condition of GMR across the momentum-/energy landscape. Second, we simulate large domains of patterns with and without strong spatial correlations, which result in improved broad-band absorptance by offering continuous bands of diffraction channels rather than discrete values as their periodic counterparts. By classifying absorbed power fractions by their in-plane momenta, we show how the PSD of the scattering layer dictates the coupling into the guided-mode regime and can substantially enhance absorptance over large spectral ranges. Third, using a combined analysis of a GMR peak in both momentum and energy space, we illustrate how mode propagation and absorption properties can be extracted directly from energy-momentum absorptance heatmaps and enable calculation of modal coupling rates. Our numerical approach thus proves a versatile tool to aid in the understanding of light coupling and absorption in complex device stacks featuring nano-patterns with arbitrary power-spectral densities and scatterer geometries. The framework is broadly applicable across photonics: any structure in which the optical response is to be decomposed into guided-mode contributions — LEDs, thermal emitters, plasmonic sensors, or solar cells

Optics EXPRESS

— benefits from this methodology. It enables the evaluation of critical physical quantities and bridges the gap between simplified analytical models and practical device optimizations.

4. Methods

Toolbox modules. The post-processing pipeline comprises six modules: (1) FDTD simulation of arbitrary 3D structures with frequency-domain power-dissipation monitors; (2) Far-field projection of the monitor spatial data; (3) Construction of $k_{\parallel}$–E_{ph} heatmaps from the spatially resolved dissipation data; (4) Internal loss decomposition to quantify light-trapping contributions to material absorption and radiative channels (reflection); (5) A peak-finding algorithm to identify guided-mode resonances or assign dispersion curves obtained from a mode solver; (6) Peak fitting to compute the resonances' physical properties such as in-plane momentum, group velocity, and external coupling rate γ_e. A minimal Python implementation of modules is provided as Supplement 1 (see Data Availability).

4.1. Simulation setup and details

Simulations are performed with the commercial software ANSYS Optics Lumerical (see Fig. 8). We use 2.5 meV resolution in photon energy and the simulations run until a predetermined auto

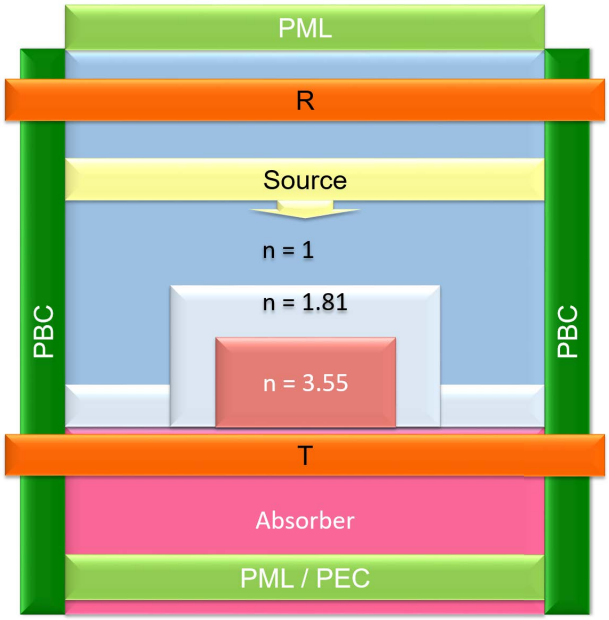

Fig. 8. Schematic of the simulation layout. The boundaries are perfectly-matched layers (PML) at the top and perfect electric conductors (PEC) or PML at the bottom, depending on the type of simulation. Periodic boundary conditions (PBC) are employed at the lateral boundaries. The source injects a plane wave downwards towards the absorber stack. Above the source, the reflection monitor R is located and transmission (T) is recorded at the top of the absorber, one mesh cell below the interface to increase numerical stability. The top interface of the absorber is decorated with the scattering layer with $n = 3.55$, which is conformally coated with an anti-reflective layer with $n = 1.81$.

shutoff level of 1×10^{-5} or less is reached. The shutoff level represents the fraction of the injected energy that has not yet been absorbed by either material or PML. The material constants of c-Si are modeled using 16 coefficients and a tolerance of 1e-4 (see Fig. 9). The mesh consists of

Optics EXPRESS

cubical Yee cells with fixed side lengths ≤ 5 nm in the pattern region, while automatic conformal meshing with a minimum mesh size ≤ 10 nm is used elsewhere. The largest simulations featuring $5 \times 5\,\mu m^2$ lateral dimension and 500 nm absorber thickness require approximately 80 GB of RAM.

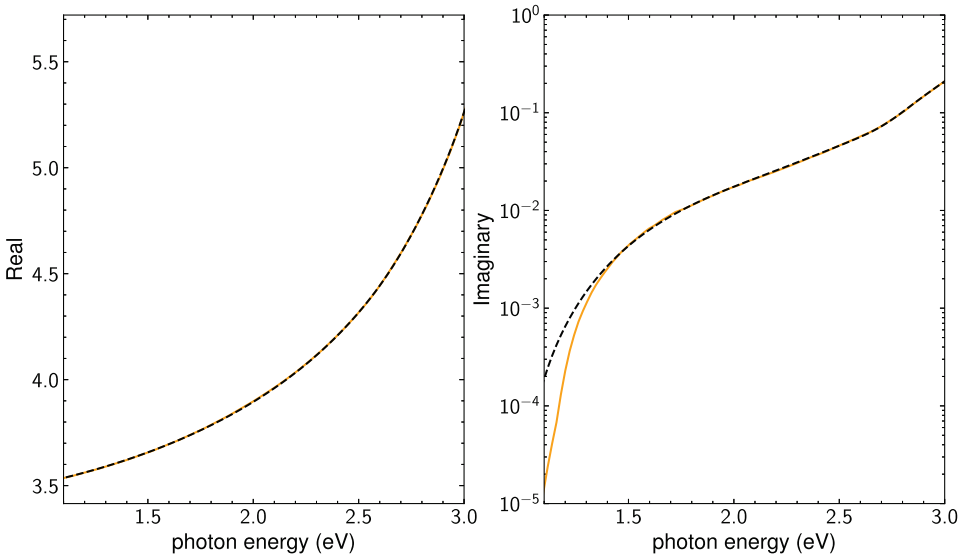

Fig. 9. Refractive index fits for silicon. The material constants are approximated using a polynomial function with 16 coefficients for the (1-3) eV range. The fit over-estimates absorption below ~ 1.3 eV, which significantly accelerates convergence at these photon energies, but has no bearing on the mutual comparability among simulations.

The finite absorbing simulations in this work feature a PEC boundary condition and are normalized to power transmitted into the substrate. The scattering layer is a non-dispersive and non-absorbing and thereby introduces artificial discontinuities of ϵ at the scatter layer - substrate interface. If instead, the scattering layer is chosen as dispersive and absorbing, transmittance differs from (1-reflectance) by the amount of (parasitic) absorption in the patterned layer, since the transmission monitor is located just below this interface. Here, we choose the non-absorbing scattering layer variant so that the power scattered into the substrate is not affected by parasitic absorption at the expense of increased reflectance by the scattering layer and n discontinuity.

Absorption in FDTD. In Lumerical FDTD, the absorbed power density (power dissipated per unit volume) is computed at each mesh cell from the time-averaged Poynting balance,

$$P_{\mathrm{abs}}(r,\omega) = -\nabla \cdot \langle \mathbf{S}(r,\omega) \rangle = \frac{\omega}{2} \operatorname{Im}\big[\varepsilon(r,\omega)\big]\, |E(r,\omega)|^2, \tag{3}$$

where $\langle \mathbf{S} \rangle = \frac{1}{2}\mathrm{Re}[\mathbf{E} \times \mathbf{H}^*]$ is the time-averaged Poynting vector and fields are phasors with $e^{-i\omega t}$ time dependence, so that $\mathrm{Im}\,\varepsilon{>}0$ denotes passive loss. This is the local form of the time-averaged Poynting theorem, exact for linear media at each frequency point. In Lumerical's implementation, $|E(r,\omega)|^2$ is taken from the steady-state field solution on a frequency-domain power monitor and $\mathrm{Im}\,\varepsilon(r,\omega)$ from the dispersive material model at each simulation frequency; the total absorbed power follows by volume integration over the semiconductor, as documented in Lumerical's Knowledge Base article "Absorption per unit volume" (https://optics.ansys.com/hc/en-us/articles/360034915653).

Optics EXPRESS

4.2. Far-field projection

The resolution in momentum (the step- or bin size) in the far field transforms is inherently limited by the simulation extent parallel to the monitor used for transformation. In the case of periodic patterns, this limit can be extended indefinitely by using multiple periods for the transformation. For aperiodic structures, however, increasing the far field periods imposes artificial diffraction orders and modifies the momentum space result.

The computational demand of the transformation is related to the number of Yee cells in the monitor data as well as the resolution chosen for the virtual screen onto which the expanded waves are projected. Hence, the resolution in the far field needs to be sufficient to account for the desired momentum resolution, which itself is limited by the lateral extend in the case of aperiodic patterns.

The finite lateral dimension gives rise to a sinc envelope in the projection, since the fields at the simulation boundaries are truncated. To ensure any ensuing line broadening is comparable for all simulation types, comparable source field dimensions are employed. Here, the number of periods and far field resolution are determined by the desired momentum resolution k_{step} according to the formula:

$$p_{\text{FF}} = 2 \times S_{\text{sourcefield}}, \tag{4}$$

with the targeted source field extent $S_{\text{sourcefield}} = 2\pi/k_{\text{step}}$. If the lateral extend (l) of an aperiodic pattern is smaller than ($S_{\text{sourcefield}}$), the number of periods is chosen as $p = S_{\text{sourcefield}}/l + 1$.

The resolution of the far field screen is determined by the required number of bins at each wavelength through the formula:

$$R_{\text{FF}} = 4 \times k_{\text{max}}/k_{\text{step}} + 1, \tag{5}$$

where $k_{\text{max}} = 2\pi n_{\text{mat}}/\lambda$ denotes the maximum wavevector of light in the material of refractive index n_{mat} in which the monitor is embedded. The pre-factor 4 is introduced to account for both positive and negative momentum values, and the maximum resolution afforded by the source field extent, while the added one results in exactly one bin at $k_{\parallel} = 0$.

The exclusion of evanescent waves proceeds as follows. The near-field data are Fourier-transformed onto the virtual monitor plane to obtain the momentum-resolved spectrum $\hat{E}(k_{\parallel})$. For each $k_{\parallel}$ component, the corresponding out-of-plane wavevector in the surrounding medium is computed as $k_z = \sqrt{n^2 k_0^2 - |k_{\parallel}|^2}$, where n is the refractive index of the substrate. If $|k_{\parallel}| < nk_0$, then k_z is real and the component is propagating in the material. If $|k_{\parallel}| > nk_0$, then k_z is imaginary and the component is evanescent and decays exponentially into the substrate. These components are set to zero and excluded from the far-field projection.

Next, the desired momentum resolution is translated into solid angle steps, in which the far field projection is integrated to obtain the fractions of power scattered up to the momentum value of each integration step. The heatmaps result from the difference between integrated far field power fractions of adjacent momentum bins and represents the total scattered power into each momentum bin.

4.3. Non-ideal back mirrors

When the back mirror has finite reflectivity or non-zero absorption, the total dissipated power splits into three contributions,

Optics EXPRESS

$$P_{\text{total}} = P_{\text{semiconductor}} + P_{\text{mirror}} + P_{\text{reflected}}, \tag{6}$$

where $P_{\text{reflected}}$ accounts for scattering back into free space. In this case, parasitic absorption by the mirror is recorded by an additional monitor and its recorded net transmission is subtracted from the absorbed power fraction used for the absorptance calculation.

4.4. GMR modal attribution

To attribute GMRs to modes obtained with the simple mode solver [39] in the presence of a distorting nanopattern, we proceed as follows: Beginning with the lowest mode order, we collect the absorptance in the $k_{\parallel}$ vicinity at each photon energy. Since a cladding with increased refractive index causes a red-shift of the modal dispersion, this implies larger $k_{\parallel}(\omega)$ of the actual modes. To accommodate the shift, we expand the integration environment asymmetrically towards the maximum in-plane momentum or the propagation constant β corresponding to the previous mode order.

For the zeroth mode, the integration interval at each $E_{\text{ph}} = \hbar c k_0$ thus comprises $\beta^0 - 2\mathrm{d}k < k_{\parallel} < k_{\text{max}} = k_0 n_{\text{mat}}$ with propagation constant β^0 from the simple mode solver for mode order 0, the momentum step size (bin size) of the heatmap $\mathrm{d}k$, and the maximum momentum k_{max} within the material of index n_{mat}. For mode order n, the interval changes to $\beta^n - 2\mathrm{d}k < k_{\parallel} < \beta^{n-1} - 2\mathrm{d}k$. In this manner, double counting of GMRs is avoided at the expense of a preference for attributing absorption to lower mode numbers. Furthermore, all power scattered into the guided mode regime will be attributed to a mode.

4.5. Random pattern generation

Coordinates are generated using the NumPy [56] random discrete number generator based on the PCG64 method. At each coordinate, a pillar is added within a $5\times5\,\mu\text{m}^2$ area until a filling fraction of approximately 50 % is achieved. In order to avoid truncation artifacts due to imposed periodic boundary conditions in the lateral direction of the simulation volume, periodic boundary conditions for the placement of pillars are employed. The finite lateral size combined with the periodic boundary conditions impose a small degree of spatial correlation [35] and artificial diffractive orders at in-plane momentum intervals of $1.26\,\mu\text{m}^{-1}$.

4.6. Peak detection and coupling condition calculation

In the slices of absorption versus momentum or energy taken from the heatmaps, peaks are detected using the RamanSPY [57] python package. In momentum space, standard Lorentzian functions are fitted to peaks with a prominence (peak amplitude over background) above 0.2 % at each photon energy, from which the key parameters center, amplitude and full-width at half-maximum (FWHM) are extracted. In energy space, we fit Eq. (2) to the peaks in order to extract γ_e, γ_i directly. We use $N = 1$ if the PSD shows no significant intensity below k_c (sub-wavelength periodicity and hyperuniform pattern). Further physical quantities are extracted by combining the fit parameters from both energy and momentum domain, such as the group velocity $v_{\text{G}} = \mathrm{d}\omega/\mathrm{d}k = \text{FWHM}_{\text{e}}/\text{FWHM}_{\text{m}}$ from the ratios of the $\text{FWHM}_{\text{e,m}}$ from fits in energy and momentum space, respectively, and in turn the mode refractive index $n_m = c/v_{\text{G}}$ with light speed in vacuum c.

Funding. SURF (EINF-9404); Dutch Research Council (VI.Vidi.203.027); European Research Council (101116984).

Optics EXPRESS

Acknowledgments. This work is part of the Dutch Research Council (NWO) and was partially performed at the research institute AMOLF and at the University of Amsterdam. This work used the Dutch national supercomputer Snellius with the support of the SURF Cooperative using grant no. EINF-9404. J.vd.G. acknowledges support from a Vidi grant (VI.Vidi.203.027) from the Dutch National Science Foundation (NWO) as well as an European Research Council Starting Grant under grant agreement no. 101116984.

Disclosures. The authors declare no conflicts of interest.

Data Availability. A full replication package including all data and analysis scripts that underlying the figures presented in this manuscript is included. We also provide with the toolkit exemplary simulation files. An implementation of toolbox modules (heatmap construction, far-field projection, loss decomposition, peak finding, and coupling analysis), together with example scripts for each of the three pattern types discussed in this work (periodic, Poissonian, hyperuniform), are available on GitHub [58].

Supplemental document. See Supplement 1 for supporting content.

References

1. E. Yik-Khoon, J. Biser, W. Cao, *et al.*, "Metalorganic vapor phase epitaxy of III-nitride light-emitting diodes on nanopatterned AGOG sapphire substrate by abbreviated growth mode," IEEE J. Sel. Top. Quantum Electron. **15**(4), 1066–1072 (2009).
2. J.-W. Pan, P.-J. Tsai, K.-D. Chang, *et al.*, "Light extraction efficiency analysis of GaN-based light-emitting diodes with nanopatterned sapphire substrates," Appl. Opt. **52**(7), 1358 (2013).
3. H. Helmers, E. Lopez, O. Höhn, *et al.*, "68.9% Efficient GaAs-based photonic power conversion enabled by photon recycling and optical resonance," Phys. Status Solidi RRL **15**(7), 2100113 (2021).
4. N. A. Kalyuzhnyy, V. M. Emelyanov, V. V. Evstropov, *et al.*, "Optimization of photoelectric parameters of InGaAs metamorphic laser (λ=1064 nm) power converters with over 50% efficiency," Sol. Energy Mater. Sol. Cells **217**, 110710 (2020).
5. F. Mooshammer, X. Xu, C. Trovatello, *et al.*, "Enabling waveguide optics in rhombohedral-stacked transition metal dichalcogenides with laser-patterned grating couplers," ACS Nano **18**(5), 4118–4130 (2024).
6. O. Kuster, Y. Augenstein, C. Rockstuhl, *et al.*, "A three-dimensional polarization-insensitive grating coupler tailored for 3D nanoprinting," arXiv (2025).
7. Q. Cai, H. You, Q. Hou, *et al.*, "Self-assembly nanopillar/superlattice hierarchical structure: boosting AlGaN crystalline quality and achieving high-performance ultraviolet avalanche photodetector," ACS Appl. Mater. Interfaces **14**(29), 33525–33537 (2022).
8. X. Guo, D. Banerjee, I. M. Asuo, *et al.*, "Plasmon-enhanced photodetectors fabricated using digital inkjet-printing on chemically nanopatterned silicon wafers," AIP Adv. **13**(5), 055309 (2023).
9. M.-H. Li, J.-J. Chen, J.-S. Chen, *et al.*, "Development of a broadband photodetector utilizing ZnO nanorods with grating structure fabricated via nanoimprint lithography," Sens. Actuators, A **375**, 115530 (2024).
10. D. Pal, T. Lopez, and A. F. Koenderink, "Metasurface-based phosphor-converted micro-LED architecture for displays-creating guided modes for enhanced directionality," ACS Nano **19**(1), 1238–1250 (2025).
11. S. Zhang, M. Liang, Y. Yan, *et al.*, "High luminous efficacy phosphor-converted mass-produced white LEDs achieved by AlN prebuffer and transitional-refraction-index patterned sapphire substrate," Nanomaterials **12**(10), 1638 (2022).
12. B.-Y. Lin, Y.-X. Lin, S.-J. Lin, *et al.*, "Highly enhanced light extraction for organic light emitting diodes by self-assembly microlens-array films," J. Lumin. **263**, 119986 (2023).
13. Y. Kuang, M. C. Van Lare, L. W. Veldhuizen, *et al.*, "Efficient nanorod-based amorphous silicon solar cells with advanced light trapping," J. Appl. Phys. **118**(18), 185307 (2015).
14. J. Buencuerpo, T. E. Saenz, M. Steger, *et al.*, "Efficient light-trapping in ultrathin GaAs solar cells using quasi-random photonic crystals," Nano Energy **96**, 107080 (2022).
15. M. S. Branham, W. Hsu, S. Yerci, *et al.*, "15.7% Efficient 10-µm-thick crystalline silicon solar cells using periodic nanostructures," Adv. Mater. **27**(13), 2182–2188 (2015).
16. I. Massiot, A. Cattoni, and S. Collin, "Progress and prospects for ultrathin solar cells," Nat. Energy **5**(12), 959–972 (2020).
17. P. Campbell and M. Keevers, "Light trapping and reflection control for silicon thin films deposited on glass substrates textured by embossing," *Conference Record of the Twenty-Eighth IEEE Photovoltaic Specialists Conference - 2000 (Cat. No.00CH37036)*. Anchorage, AK, USA, 2000; pp. 355–358.
18. A. Cordaro, J. Van De Groep, S. Raza, *et al.*, "Antireflection high-index metasurfaces combining Mie and Fabry-Pérot resonances," ACS Photonics **6**(2), 453–459 (2019).
19. H. A. Atwater and A. Polman, "Plasmonics for improved photovoltaic devices," Nat. Mater. **9**(3), 205–213 (2010).
20. P. Molet, J. L. Garcia-Pomar, C. Matricardi, *et al.*, "Ultrathin semiconductor superabsorbers from the visible to the near-infrared," Adv. Mater. **30**(9), 1705876 (2018).
21. M. Elshorbagy, K. Abdel-Hady, H. Kamal, *et al.*, "Broadband anti-reflection coating using dielectric Si3N4 nanostructures. Application to amorphous-Si-H solar cells," Opt. Commun. **390**, 130–136 (2017).
22. S. T. Ha, Q. Li, J. K. W. Yang, *et al.*, "Optoelectronic metadevices," Science **386**(6725), eadm7442 (2024).
23. W. Wang and L. Qi, "Light management with patterned micro- and nanostructure arrays for photocatalysis, photovoltaics, and optoelectronic and optical devices," Adv. Funct. Mater. **29**(25), 1807275 (2019).

Optics EXPRESS

24. M. A. Green, "Lambertian light trapping in textured solar cells and light-emitting diodes: analytical solutions," Prog. Photovoltaics **10**(4), 235–241 (2002).
25. Z. Yu, A. Raman, and S. Fan, "Fundamental limit of nanophotonic light trapping in solar cells," Proc. Natl. Acad. Sci. **107**(41), 17491–17496 (2010).
26. A. Naqavi, F.-J. Haug, C. Battaglia, *et al.*, "Light trapping in solar cells at the extreme coupling limit," J. Opt. Soc. Am. B **30**(1), 13 (2013).
27. S. Collin and M. Giteau, "Upper bounds on broadband absorption," arXiv (2024).
28. M. Florescu, S. Torquato, and P. J. Steinhardt, "Designer disordered materials with large, complete photonic band gaps," Proc. Natl. Acad. Sci. **106**(49), 20658–20663 (2009).
29. N. Tavakoli, R. Spalding, A. Lambertz, *et al.*, "Over 65% sunlight absorption in a 1 um Si Slab with hyperuniform texture," ACS Photonics **9**(4), 1206–1217 (2022).
30. P. M. Piechulla, E. Slivina, D. Bätzner, *et al.*, "Antireflective huygens' metasurface with correlated disorder made from high-index disks implemented into silicon heterojunction solar cells," ACS Photonics **8**(12), 3476–3485 (2021).
31. H. Hauser, K. Mühlbach, O. Höhn, *et al.*, "Tailored disorder: a self-organized photonic contact for light trapping in silicon-based tandem solar cells," Opt. Express **28**(8), 10909 (2020).
32. M.-C. Van Lare and A. Polman, "Optimized scattering power spectral density of photovoltaic light-trapping patterns," ACS Photonics **2**(7), 822–831 (2015).
33. S. S. Wang, M. G. Moharam, R. Magnusson, *et al.*, "Guided-mode resonances in planar dielectric-layer diffraction gratings," J. Opt. Soc. Am. A **7**(8), 1470 (1990).
34. G. R. Neupane, J. F. Roller, S. M. Thon, *et al.*, "Insights into transient photovoltage lifetimes via dark *J-V* analysis in perovskite solar cells," J. Phys. Chem. C **128**(39), 16372–16379 (2024).
35. P. Lalanne, M. Chen, C. Rockstuhl, *et al.*, "Disordered optical metasurfaces: basics, properties, and applications," Adv. Opt. Photonics **17**(1), 45 (2025).
36. J. P. Hugonin and P. Lalanne, "RETICOLO software for grating analysis," arXiv (2021).
37. Institut Optique Graduate School, LP2N, CNRS RETOP: near-to-far-field transformation for radiation planewaves and guided modes (Version 10). 2025; https://zenodo.org/doi/10.5281/zenodo.14633602.
38. T. Wu and P. Lalanne, "Rigorous electromagnetic quasinormal-mode method made easy for users," Laser Photonics Rev. **20**(14), e03045 (2026).
39. A. Lambertz, Modesolver and absorption calculator. 2021; https://github.com/shibmaster/modesolver-absorption.
40. G. XII. Maxwell, "Colours in metal glasses and in metallic films," Philosophical Transactions of the Royal Society of London. Series A, Containing Papers of a Mathematical or Physical Character **203**, 385–420 (1904).
41. E. Allahyarov, "Theoretical study of nanocomposite permittivity with a tunable clustering of inclusions," Adv. Theory Simul. **3**(5), 2000005 (2020).
42. E. Yablonovitch, "Statistical ray optics," J. Opt. Soc. Am. **72**(7), 899 (1982).
43. J. Van De Groep and A. Polman, "Designing dielectric resonators on substrates: combining magnetic and electric resonances," Opt. Express **21**(22), 26285 (2013).
44. H. A. Haus, *Waves and fields in optoelectronics* (Prentice-Hall series in solid state physical electronics; Prentice-Hall, 1984).
45. I. Simonsen, A. Larsen, E. Andreassen, *et al.*, "Haze of surface random systems: an approximate analytic approach," arXiv (2009).
46. S. Torquato and F. H. Stillinger, "Local density fluctuations, hyperuniformity, and order metrics," Phys. Rev. E **68**(4), 041113 (2003).
47. R. D. Batten, F. H. Stillinger, and S. Torquato, "Classical disordered ground states: super-ideal gases and stealth and equi-luminous materials," J. Appl. Phys. **104**(3), 033504 (2008).
48. M. A. Bishop, S. Oughton, T. N. Parashar, *et al.*, "Direct power spectral density estimation from structure functions without Fourier transforms," Phys. Fluids **38**(2), 025107 (2026).
49. R. H. Siddique, Y. J. Donie, G. Gomard, *et al.*, "Bioinspired phase-separated disordered nanostructures for thin photovoltaic absorbers," Sci. Adv. **3**(10), e1700232 (2017).
50. A. Bozzola, M. Liscidini, and L. C. Andreani, "Broadband light trapping with disordered photonic structures in thin-film silicon solar cells," Prog. Photovoltaics **22**(12), 1237–1245 (2014).
51. I. Massiot, C. Colin, C. Sauvan, *et al.*, "Multi-resonant absorption in ultra-thin silicon solar cells with metallic nanowires," Opt. Express **21**(S3), A372 (2013).
52. T. Khaleque and R. Magnusson, "Light management through guided-mode resonances in thin-film silicon solar cells," J. Nanophotonics **8**(01), 1–14 (2014).
53. K. Söderström, F.-J. Haug, J. Escarré, *et al.*, "Photocurrent increase in n-i-p thin film silicon solar cells by guided mode excitation via grating coupler," Appl. Phys. Lett. **96**(21), 213508 (2010).
54. C. Trompoukis, I. Massiot, V. Depauw, *et al.*, "Disordered nanostructures by hole-mask colloidal lithography for advanced light trapping in silicon solar cells," Opt. Express **24**(2), A191 (2016).
55. A. P. Vafa, S. R. P. Silva, and M. Florescu, "Balancing order and disorder: optimal light trapping in ultrathin silicon photovoltaics," Optica **13**(6), 1118 (2026).
56. C. R. Harris, K. J. Millman, S. J. van der Walt, *et al.*, Array programming with NumPy. 2020; https://www.nature.com/articles/s41586-020-2649-2.

Optics EXPRESS

57. D. Georgiev, S. V. Pedersen, R. Xie, *et al.*, "An open-source Python package for integrative Raman spectroscopy data analysis," arXiv (2023).
58. A. Lambertz, Mode Coupling Toolbox. GitHub repository, 2026; https://github.com/alambertz/mode-coupling-toolbox, ANSYS-Lumerical FDTD simulation setup and post-processing pipeline for quantifying light coupling to guided modes in semiconductor slabs with arbitrary scattering patterns. Accessed September 8, 2026.